Earth and Planetary Science Letters 418 (2015) 126–135

Contents lists available at ScienceDirect

Earth and Planetary Science Letters

www.elsevier.com/locate/epsl

Olivine and pyroxene from the mantle of asteroid 4 Vesta

Nicole G. Lunning [a,*], Harry Y. McSween Jr. [a,1], Travis J. Tenner [b,2], Noriko T. Kita [b,3], Robert J. Bodnar [c,4]

[a] Department of Earth and Planetary Sciences and Planetary Geosciences Institute, University of Tennessee, Knoxville, TN 37996, USA
[b] Department of Geosciences, University of Wisconsin, Madison, WI 53706, USA
[c] Department of Geosciences, Virginia Tech, Blacksburg, VA 24061, USA

ARTICLE INFO

Article history:
Received 25 September 2014
Received in revised form 25 February 2015
Accepted 25 February 2015
Available online 17 March 2015
Editor: T. Mather

Keywords:
planetary formation
howardites–eucrite–diogenite (HED)
meteorites
planetesimals
asteroids
magma ocean
partial melting

ABSTRACT

A number of meteorites contain evidence that rocky bodies formed and differentiated early in our solar system's history, and similar bodies likely contributed material to form the planets. These differentiated rocky bodies are expected to have mantles dominated by Mg-rich olivine, but direct evidence for such mantles beyond our own planet has been elusive. Here, we identify olivine fragments (Mg# = 80–92) in howardite meteorites. These Mg-rich olivine fragments do not correspond to an established lithology in the howardite–eucrite–diogenite (HED) meteorites, which are thought to be from the asteroid 4 Vesta; their occurrence in howardite breccias, combined with diagnostic oxygen three-isotope signatures and minor element chemistry, indicates they are vestan. The major element chemistry of these Mg-rich olivines suggests that they formed as mantle residues, in crustal layered intrusions, or in Mg-rich basalts. The trace element chemistry of these Mg-rich olivines supports an origin as mantle samples, but other formation scenarios could be possible. Interpreted as mantle samples, the range of Mg-rich olivine compositions indicates that Vesta's structure differs from that predicted by conventional models: Vesta has a chemically heterogeneous mantle that feeds serial magmatism. The range of olivine major element chemistries is consistent with models of an incompletely melted mantle such as in the model proposed by Wilson and Keil (2013) rather than a whole-mantle magma ocean for Vesta. Trace element chemistries of Mg-rich pyroxenes (Mg# = 85–92) provide support that some of these pyroxenes may represent initial fractional crystallization of mantle partial melts.

1. Introduction

Meteorites can sample separate portions of differentiated asteroidal bodies; for instance, iron meteorites represent cores and basaltic achondrites correspond to crusts. While meteorite collections include samples that originate from up to 150 chemically distinct parent bodies (Burbine et al., 2002), those representing the ultramafic mantles of differentiated asteroids are rare. Most mantle samples should be characterized by Mg-rich olivine, based on redox conditions inferred from crustal meteorite assemblages, and assuming a chondritic bulk composition. The only meteorite examples are pallasites, which may be derived from mantle–core boundaries, and are not tied to any known crustal meteorite groups (Burbine et al., 2002). Mantle lithologies are also rare as collisional fragments in the asteroid belt (Sunshine et al., 2007). The rarity of mantle material, combined with the relative abundance of differentiated samples represented by crustal and core material, has confounded researchers.

One plausible location to search for samples containing mantle material is asteroid 4 Vesta, where the impact that created the Rheasilvia basin excavated to mantle depths of 60–100 km (McSween et al., 2013a; Jutzi et al., 2013). However, olivine has not been detected in this basin, possibly because modest amounts of coarse-grained olivine (≤30%) are easily masked by orthopyroxene in visible/near-infrared spectra (Beck et al., 2013a). Although olivine-rich areas have been identified elsewhere on Vesta, the related olivine chemistry has not been determined and the related geologic context is not consistent with mantle material (Ammannito et al., 2013). The most abundant samples sourced from a differentiated body are the howardite, eucrite, and diogenite (HED) meteorites. HEDs are interpreted to represent samples of the crust of Vesta and possibly its upper mantle, based on numerous observations (McSween et al., 2013b); furthermore, the orbital

* Corresponding author. Tel.: +1 865 974 5324.
E-mail addresses: nlunning@utk.edu (N.G. Lunning), mcsween@utk.edu (H.Y. McSween Jr.), tenner@wisc.edu (T.J. Tenner), noriko@geology.wisc.edu (N.T. Kita), rjb@vt.edu (R.J. Bodnar).
[1] Tel.: +1 865 974 9805.
[2] Tel.: +1 806 890 1347.
[3] Tel.: +1 608 262 7118.
[4] Tel.: +1 540 231 7455.

http://dx.doi.org/10.1016/j.epsl.2015.02.043
0012-821X/

distribution of Vesta-like asteroids in the asteroid belt is consistent with their ejection from Vesta during the impact that produced the Rheasilvia basin. Relatively small Vesta-like asteroids routinely cross Earth's orbital path and become meteorites. The vestan meteorites include a wide range of igneous lithologies, including eucrites (basalts and gabbros), and diogenites (orthopyroxenites, harzburgites). The howardites are brecciated samples of Vesta's regolith and megaregolith (e.g., Cartwright et al., 2014). Howardites incorporate fragments of eucrites, diogenites, impact-derived materials, exogenic chondritic components, and rare lithologies of undetermined provenance (e.g., Barrat et al., 2012). In this study, we investigate the provenance and petrogenesis of a howardite component of unknown origin: olivine and pyroxene fragments that are more Mg-rich than similar phases occurring in eucrite or diogenite meteorites.

2. Materials and methods

2.1. Meteorite samples

The 4 howardites in this study were all found within a ~4 km area in the Grosvenor Mountains field area (GRO) in Antarctica. These howardites—GRO 95534, GRO 95535, GRO 95574, GRO 95581—were proposed as a pairing group in their initial descriptions. Their pairing is also supported by similarities in their bulk geochemistry. Based on solar wind concentrations, these paired howardites formed from regolith that was exposed on an asteroid's surface, rather than from buried megaregolithic material (Cartwright et al., 2014).

The following howardite thin sections were analyzed in this study: GRO 95534,4; GRO 95535,16; GRO 95574,17; and GRO 95581,7. They all contain Mg-rich olivine of unknown provenance, as well as less magnesian olivine grains having compositions typically associated with diogenites (Beck and McSween, 2010). To evaluate the consistency of our methods with previous oxygen isotope analyses on HED meteorites using laser fluorination analytical methods, we also analyzed diogenite-composition olivine in the howardites and two diogenites: GRA 98108,16 and LEW 88008,14, which respectively represent meteorites found in the Graves Nunataks (GRA) and Lewis Cliff (LEW) sites in Antarctica.

2.2. Major element analyses & quantitative modal analyses

Electron microprobe analyses (EMPA) were performed with a Cameca SX-100 EMP at the University of Tennessee using wavelength-dispersive spectrometry (WDS). The mineral spot analyses were conducted with a 1 μm beam at the following conditions: 15 kV and 30 nA for olivine, and 20 kV and 100 nA for pyroxene. Analyses used PAP corrections. Natural and synthetic standards were analyzed daily, and ≥99% consistency with standards was maintained. The 3σ detection limits for 20 kV and 100 nA EMPA on olivine (Table 1) are as follows or lower (in ppm): Si 136, Mn 80, Fe 123, Mg 179, Al 122, Ca 120, Ti 77, Ni 44, Cr 111. The 3σ detection limits for 15 kV and 30 nA EMPA on pyroxene (Table 2) are as follows or lower (in ppm): Si 202, Na 243, Mn 249, Fe 349, Cr 249, Al 154, Ca 213, Ti 212, Mg 211, K 242. We calculated Mg# = Mg/(Mg + Fe) values from our molar EMPA data.

The 4 howardite thin sections were mapped with WDS for 8 elements: Mg, Si, Fe, Al, Ca, Cr, K (K-lines) and Ni (L-line). EDS (energy-dispersive spectrometry) x-ray maps were collected simultaneously for S and Ti. Using methods similar to those of Beck et al. (2012), we constructed lithologic distribution maps with ENVI 4.2 software to locate olivine and pyroxene grains with Mg-rich compositions. The 10 x-ray maps were assembled into a multispectral image cube for each thin section. Regions of interest (ROIs) were defined based on mineral spot analyses for specific minerals or ranges of mineral chemistries. These ROIs and minimum distance classification were used to map the distribution of each phase (defined by ROIs) in these howardites, including those relevant to this study: Mg-rich olivine, diogenite olivine, and Mg-rich orthopyroxene. Grains of interest identified by our lithologic distribution mapping were analyzed by EMP prior to oxygen isotope and/or trace element analysis.

2.3. Oxygen isotope analyses

In situ oxygen three-isotope analyses were conducted on a Cameca IMS 1280, a large-radius double-focusing secondary ion mass-spectrometer at the WiscSIMS Laboratory, University of Wisconsin, Madison. Analytical conditions and data reduction are similar to those of Kita et al. (2010) and Tenner et al. (2013). The primary Cs^+ beam was focused to a 15 μm diameter spot with an intensity of 3 nA. The oxygen isotope data are reported relative to the standard Vienna Mean Ocean Water (VSMOW) using delta notation: $\delta^{17}O = [(^{17}O/^{16}O)_{sample}/(^{17}O/^{16}O)_{VSMOW} - 1] \times 1000$; $\delta^{18}O = [(^{18}O/^{16}O)_{sample}/(^{18}O/^{16}O)_{VSMOW} - 1] \times 1000$; and $\Delta^{17}O$ is defined as $\delta^{17}O - 0.52 \times \delta^{18}O$, representing the displacement from the terrestrial fractionation line (TFL).

Matrix effects were evaluated from olivine standards (Fo_{60}, Fo_{89}, and Fo_{100}) and instrumental biases of unknowns were corrected as a function of their Fo contents as determined by EMPA. Four bracket analyses on the San Carlos olivine (Fo_{89}) standard were completed before and after sets of 12 unknown analyses. Typical reproducibility (spot-to-spot or 2σ standard deviation; 2SD) of San Carlos olivine standard was ~0.3‰ for $\delta^{18}O$, $\delta^{17}O$, and $\Delta^{17}O$. A total of 81 unknown spot analyses were collected on 30 separate olivine grains in the howardite and diogenite thin sections: 14 of the grains were diogenite composition olivine (Mg# = 61–79) and 16 were Mg-rich olivine (Mg# = 80–92). Between 1 and 6 spots were measured per olivine grain. Available flat fracture-free areas large enough to accommodate the 15 μm spot analysis dictated the number of spots per grain. The oxygen three-isotope contents of diogenite composition olivine fragments in the GRO 95 howardites were measured along with the Mg-rich olivine fragments. Most oxygen isotope analyses of HED meteorites have been on bulk rock samples and, to our knowledge, no *in situ* SIMS analyses of oxygen isotopes in HED minerals have been published. Thus, we analyzed diogenite olivine to independently determine the oxygen three-isotopic composition of slowly cooled HED (vestan) olivine. The average $\Delta^{17}O$ compositions were calculated for Mg-rich olivine ($n = 47$) and diogenite olivine ($n = 34$), respectively. The 2σ standard errors of the means of both unknowns and San Carlos olivine standard ($n = 40$) were propagated into the final uncertainties of the average $\Delta^{17}O$ compositions.

2.4. Trace element analyses

In situ trace element analyses were conducted at Virginia Tech using an Agilent 7500ce inductively coupled plasma mass spectrometer (ICP-MS) combined with an Excimer 193 nm ArF GeoLasPro Laser Ablation (LA) system. Laser spot sizes of 16–60 μm were used to analyze single-phase olivine or pyroxene. We analyzed 13 Mg-rich olivine grains and 4 Mg-rich pyroxene grains in the GRO 95 howardites. Between 1 and 5 spots were measured per mineral grain. Available flat fracture-free areas dictated the size and number of spots on each grain. The external standard used was NIST SRM610 reference glass. Every 2 hr, we measured the NIST standard twice for 60 s to correct for drift. For each of the analyses, approximately 60 s of background signal was collected before the ablation process was initiated. Sample ablation times ranged from 30–50 s using a laser repetition rate of 5 Hz. The

Table 1
Electron microprobe analyses of Mg-rich olivine from GRO 95 howardites.

GRO 95534,4										
Grain	Ol5	Ol8	Ol14	Ol6	Ol10	Ol9	Ol1	Ol11	Ol12	Ol13
n	2	1	1	2	1	1	14	1	1	1
SiO_2	40.7	39.9	40.1	40.0	40.2	40.0	38.8	39.7	39.1	38.8
TiO_2	b.d.	0.05	b.d.	b.d.	b.d.	b.d.	b.d.	b.d.	0.015	b.d.
Al_2O_3	0.02	0.07	0.03	0.03	0.03	b.d.	b.d.	b.d.	0.08	0.03
Cr_2O_3	0.07	0.05	0.06	0.05	0.07	0.04	0.03	0.04	0.12	0.15
MgO	49.9	47.3	47.8	47.5	47.4	47.2	46.6	45.9	43.0	42.2
CaO	0.09	0.07	0.04	0.05	0.08	0.07	0.05	0.09	0.12	0.12
MnO	0.19	0.27	0.29	0.29	0.29	0.29	0.30	0.33	0.40	0.42
FeO	8.7	11.5	11.7	11.9	12.1	12.5	12.7	14.1	17.3	18.4
NiO	b.d.	b.d.	b.d.	b.d.	b.d.	b.d.	b.d.	b.d.	0.006	b.d.
Total	99.6	99.3	99.9	99.8	100.2	100.2	98.5	100.1	100.1	100.1
Mg#	91.1	88.0	88.0	87.7	87.5	87.1	86.7	85.3	81.6	80.3
Fe/Mn	44.6	42.1	39.9	40.9	40.8	41.9	41.5	42.6	42.8	43.5

GRO 95535,16				
Grain	Ol12	Ol14	Ol9	Ol17
n	2	2	1	1
SiO_2	40.5	40.3	40.3	39.7
TiO_2	b.d.	b.d.	b.d.	0.016
Al_2O_3	0.03	0.02	0.02	b.d.
Cr_2O_3	0.08	0.14	0.12	0.05
MgO	50.0	49.1	48.6	46.1
CaO	0.06	0.07	0.07	0.05
MnO	0.21	0.23	0.28	0.34
FeO	8.8	9.7	11.5	14.0
NiO	b.d.	0.008	b.d.	b.d.
Total	99.7	99.5	100.9	100.2
Mg#	91.0	90.1	88.3	85.5
Fe/Mn	40.5	41.4	40.6	40.2

GRO 95574,17						
Grain	Ol13	Ol8	Ol1	Ol15	Ol6	Ol18
n	2	3	5	3	4	2
SiO_2	40.9	40.6	40.4	39.8	39.3	39.0
TiO_2	b.d.	b.d.	b.d.	b.d.	b.d.	0.014
Al_2O_3	0.04	0.03	0.02	0.03	0.03	0.03
Cr_2O_3	0.14	0.09	0.04	0.08	0.14	0.08
MgO	49.7	49.1	49.0	46.4	44.8	44.0
CaO	0.12	0.07	0.04	0.07	0.07	0.08
MnO	0.22	0.24	0.24	0.31	0.36	0.39
FeO	8.9	9.4	9.6	13.1	15.3	16.5
NiO	b.d.	b.d.	b.d.	b.d.	b.d.	b.d.
Total	100.0	99.5	99.4	99.8	100.0	100.1
Mg#	90.8	90.3	90.1	86.3	84.0	82.6
Fe/Mn	40.0	39.3	39.6	41.7	42.3	42.3

GRO 95581,7								
Grain	Ol9	Ol18	Ol14	Ol19	Ol1	Ol17	Ol5	[a]Ol in MgPx1
n	1	1	1	1	5	1	1	1
SiO_2	40.6	40.1	39.9	40.0	39.8	39.2	38.9	40.7
TiO_2	b.d.	b.d.	b.d.	b.d.	b.d.	b.d.	b.d.	b.d.
Al_2O_3	0.03	0.02	0.03	0.03	0.03	0.03	0.11	b.d.
Cr_2O_3	0.09	0.05	0.12	0.06	0.11	0.11	0.06	0.05
MgO	50.4	48.1	47.8	47.6	46.9	44.4	43.2	47.6
CaO	0.07	0.07	0.11	0.07	0.09	0.11	0.15	0.03
MnO	0.22	0.28	0.29	0.29	0.32	0.37	0.41	0.30
FeO	8.4	11.7	11.6	12.0	12.6	16.2	17.0	12.8
NiO	b.d.	b.d.	b.d.	b.d.	b.d.	0.007	b.d.	n.d.
Total	99.8	100.2	99.9	100.1	99.8	100.5	99.8	101.4
Mg#	91.5	88.0	88.0	87.7	86.9	83.0	81.9	86.9
Fe/Mn	36.9	40.8	40.2	41.3	39.1	43.0	40.4	43.7

[a] Note: the grain 'Ol in MgPx1' in howardite GRO 95581,17 was analyzed with the conditions described for pyroxene.

samples were ablated in a helium atmosphere. The helium gas carrying the ablated particles was then mixed with the make-up gas (argon) before entering the ICP-MS system. The 3σ analytical precision for the LA-ICP-MS system for the elements analyzed in this study (compared to NIST612) is better than $\pm 5\%$ relative (for V, Co, Cr, Ce, Zn, Ga); between ± 5 and 10% (for Ni, Rb, Nb, Sr, Ba, Pr, Eu, Hf, Pb); between ± 10 and 20% (for Y, Zr, La, Nd, Sm, Gd, Dy, Er, Yb, Ta, Lu, Th, Tb, Ho, U), and poorer than $\pm 20\%$ (Sc). Analytical precision was determined previously using the NIST standard 610 as the reference, and then USGS standards BCR-2G, BHVO-2G, BIR-1G, NKT-1G and NIST standards (NIST612 and NIST614) were analyzed according to established analytical protocols. USGS standards BCR-2G, BHVO-2G and BIR-1G were prepared from natural basalt glasses, and NKT-1G was prepared from a natural nephelinite glass. Details of the analytical results related to these analyses are available at: http://www.geochem.geos.vt.edu/fluids/laicpms/VT_LAICPMS_Accuracy_Precision.pdf.

The LA-ICP-MS detection limits are dependent on several factors, such as the element (isotope) being measured, spot size, and duration of the analysis. Therefore, each analysis and element has a different detection limit. For all of the trace elements listed above, the detection limits obtained during our calibration runs were always less than 1 ppm. Data reduction for all analyses was conducted with both the Analysis Management System (AMS) software (Mutchler et al., 2008) and the SILLS software program (Guillong et al., 2008), both enabling time-resolved signal analysis. We reduced the data with the SILLS software program to calculate the 1σ error and limit of detection. Concentrations calculated by each of these programs were consistent.

Time-resolved signal analysis provides easy recognition of sample heterogeneities during the ablation process, such as when traversing from one phase into a different phase during ablation, or if a solid inclusion is included in the ablated material. These software packages allow the user to select a portion of the ablation signal to process and eliminate signal from multiple phases in order to obtain the composition of only the phase of interest.

3. Results

3.1. Description of Mg-rich olivine and pyroxene

The Mg-rich olivine and Mg-rich pyroxene in this study are all fragmental grains. They are surrounded by a diverse range of other fragmental grains or clasts, and the Mg-rich olivines and pyroxenes exhibit no compositional or textural evidence of chemical equilibration with the surrounding material. The fragmental material in these howardites is predominately from HED lithologies, although, exogenic carbonaceous chondrite clasts do occur. There is no apparent spatial correlation between the Mg-rich olivines and/or Mg-rich pyroxenes, which appear to be randomly distributed in the thin sections. The Mg-rich olivine and pyroxene grains are accessory components within the GRO 95 howardites.

The Mg-rich olivines and pyroxenes are irregularly-shaped mineral fragments. The largest Mg-rich olivine grain we found is close to 1 mm in its longest dimension (Fig. 1a); the rest of the Mg-rich olivines are between 50–200 μm in their longest dimension. Most of the Mg-rich pyroxene grains also are between 50–200 μm in their longest dimension, but two are larger: a grain in GRO 95574,17 (MgPx1) is close to 400 μm in its longest dimension (Fig. 1b) and a grain in GRO 95535,16 (MgPx2) is about 700 μm in its longest dimension.

Both the Mg-rich olivine and pyroxene commonly display undulatory extinction and are crosscut by fractures (Fig. 1). In some of the larger grains planar fracturing is evident, but most grains are too small for a pervasive fracture pattern to be observed. A few grains contain small opaque inclusions, but most are inclusion-free. The olivine and pyroxene grains do not appear to be altered or cor-

Table 2
Electron microprobe analyses of Mg-rich pyroxene from the GRO 95 howardites.

GRO 95*	534,4	574,17	581,7	581,7	535,16	574,17	581,7	535,16	574,17	535,16	574,17	534,4	581,7	535,16	535,16	535,16	535,16
Grain	MgPx8	MgPx1	MgPx8	MgPx1	MgPx5	MgPx5	MgPx2	MgPx8	MgPx3	MgPx3	MgPx2	MgPx2	MgPx4	MgPx6	MgPx2	MgPx13	MgPx1
n	2	4	1	3	3	4	1	1	2	2	2	3	1	1	3	1	1
SiO_2	57.3	56.3	58.0	57.9	57.6	57.4	57.2	56.3	56.8	57.0	56.9	56.8	56.1	56.7	56.5	56.6	56.6
TiO_2	0.16	0.09	b.d.	b.d.	0.04	b.d.	b.d.	0.08	b.d.	0.04	b.d.	0.04	0.11	b.d.	0.05	0.05	b.d.
Al_2O_3	1.13	1.60	0.29	0.13	0.18	0.11	0.50	0.91	0.37	0.45	0.26	0.42	1.02	0.31	0.49	0.59	0.41
Cr_2O_3	0.66	0.91	0.46	0.29	0.26	0.16	0.65	0.85	0.54	0.72	0.44	0.81	0.62	0.63	0.71	0.56	0.54
MgO	35.1	33.7	35.0	34.6	34.4	33.8	32.8	32.2	32.7	32.8	32.9	32.4	31.9	32.3	31.9	32.3	32.2
CaO	1.13	1.18	0.32	0.29	0.27	0.25	0.53	1.08	0.81	0.53	0.26	0.46	1.27	0.41	0.68	0.53	0.49
MnO	0.24	0.26	0.25	0.29	0.32	0.35	0.32	0.38	0.36	0.32	0.32	0.34	0.41	0.31	0.33	0.34	0.35
FeO	5.49	6.52	7.11	7.75	8.21	8.79	9.00	9.17	9.42	9.58	9.73	9.88	9.75	10.08	10.02	10.28	10.25
Na_2O	b.d.	b.d.	b.d.	b.d.	b.d.	b.d.	b.d.	b.d.	b.d.	b.d.	b.d.	b.d.	b.d.	b.d.	b.d.	b.d.	b.d.
K_2O	b.d.	b.d.	b.d.	b.d.	b.d.	b.d.	b.d.	b.d.	b.d.	b.d.	b.d.	b.d.	b.d.	b.d.	b.d.	b.d.	b.d.
Total	101.26	100.61	101.47	101.30	101.29	100.87	101.00	101.01	101.05	101.39	100.89	101.24	101.18	100.80	100.70	101.23	100.89
Mg#	91.9	90.2	89.8	88.8	88.2	87.3	86.6	86.2	86.1	85.9	85.8	85.4	85.4	85.1	85.0	84.8	84.8
Fe/Mn	23.0	25.3	28.6	26.0	25.5	25.2	28.1	23.9	25.9	29.6	30.0	28.8	23.5	31.7	30.3	29.7	29.0
En	90.0	88.2	89.2	88.4	87.8	86.9	85.8	84.5	84.8	85.1	85.3	84.7	83.3	84.4	83.9	84.0	84.0
Fs	7.9	9.6	10.2	11.1	11.7	12.7	13.2	13.5	13.7	14.0	14.2	14.5	14.3	14.8	14.8	15.0	15.0
Wo	2.1	2.2	0.6	0.5	0.5	0.5	1.0	2.0	1.5	1.0	0.5	0.9	2.4	0.8	1.3	1.0	0.9

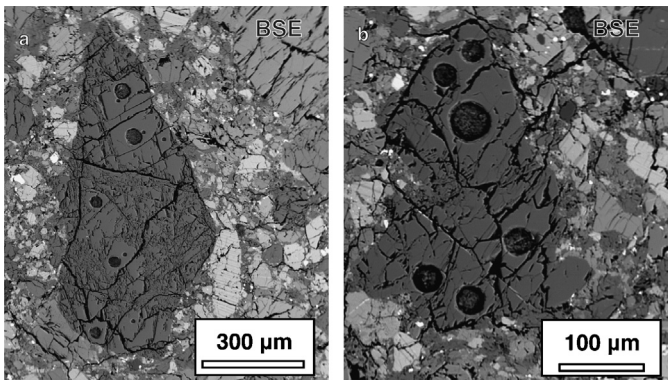

Fig. 1. Backscatter electron (BSE) images of fragmental Mg-rich olivine and pyroxene grains. a.) Mg-rich olivine fragment (Mg# 90.1) from GRO 95574,17 with LA-ICP-MS pits (32–44 µm laser spots) and SIMS pits (15-µm beam spots). b.) Mg-rich pyroxene fragment (Mg# 90.2) from GRO 95574,17 with LA-ICP-MS pits (24–44 µm laser spots).

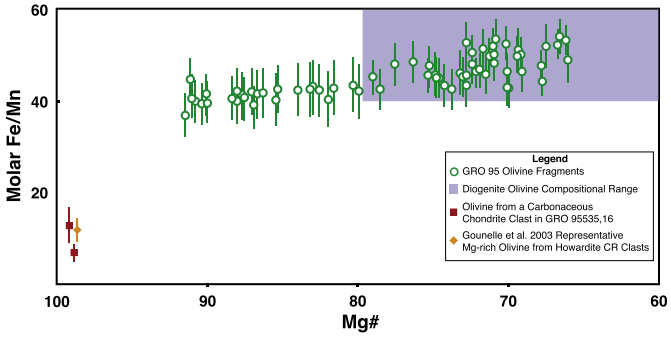

Fig. 2. Fe/Mn ratio versus Mg# of fragmental olivine grains from the GRO 95 howardites. Each green open circle corresponds to an individual olivine fragment; where multiple analyses were collected the symbol corresponds to an average value. Olivines in a carbonaceous chondrite clast in GRO 95535,16 were measured in this study. The representative composition of olivine in CR chondrite clasts in the howardite Kapoeta is calculated from data in Gounelle et al. (2003). Error bars are the propagated analytical error on Mn. The diogenite compositional field is based on published data (Beck et al., 2012; Mittlefehldt et al., 1998).

roded under plane polarized light microscopy. We looked for but did not find any terrestrial weathering byproducts such as calcite or gypsum in our thin sections.

3.2. Major element analyses

Each grain we studied is compositionally homogeneous based on multiple EMPA when size and fracturing permitted, and by observations using backscattered electron microscopy. The Mg-rich olivine fragments have Mg# = 80–92 and Fe/Mn = 37–45. Mg-rich pyroxenes have Mg# = 85–92 and Fe/Mn = 23–40 (Fig. 2, Tables 1 and 2).

3.3. Oxygen isotope analyses of olivine

The weighted average of the oxygen three-isotope analyses of Mg-rich olivine grains ($n = 16$) is $\delta^{18}O = 3.49 \pm 0.32‰$ and $\delta^{17}O = 1.50 \pm 0.17‰$. The unweighted average of all Mg-rich olivine oxygen isotope spot analyses ($n = 47$) is $\Delta^{17}O = -0.295 \pm 0.080‰$. The weighted average of all diogenite olivine grains ($n = 14$) analyzed is $\delta^{18}O = 3.25 \pm 0.33‰$ and $\delta^{17}O = 1.41 \pm 0.31‰$. The unweighted average of all diogenite olivine spot analyses ($n = 34$) is $\Delta^{17}O = -0.259 \pm 0.077‰$.

These diogenite analyses, which were conducted for the purpose of methods testing, demonstrate that *in situ* SIMS analyses of diogenite olivine yield results (Figs. 4 and A.1, Tables A.1–2)

Table 3
Ni and Co concentrations for Mg-rich olivine from GRO 95 howardites. Abridged LA ICP-MS data, Table A.5 includes extended trace element data for each grain. 1σ refers to the error of the analyses calculated by the SILLS program using the Longerich method (Guillong et al., 2008). 1σ is given in terms of the last decimal place, for instance 34.4 ± 4.7 is listed as 34.4 (47). Mg# listed in this table were calculated from EMPA data (Table 1).

	GRO 95534,4								GRO 95535,16			
Grain	Ol5		Ol9		Ol1		Ol6		Ol14		Ol9	
Mg#	91.1		87.1		86.7		87.7		90.1		88.3	
	µg/g	1σ	µg/g	1σ	µg/g	1σ	µg/g	1σ	µg/g	1σ	µg/g	1σ
Ni	34.4	(47)	10.1	(38)	14.1	(19)	18	(5)	52	(4)	30	(4)
Co	16.2	(6)	12.2	(6)	14.2	(3)	5.2	(5)	26	(1)	25	(1)

	GRO 95574,17								GRO 95581,7					
Grain	Ol8		Ol1		Ol15		Ol6		Ol9		Ol18		Ol1	
Mg#	90.3		90.1		86.3		84		91.5		88		86.9	
	µg/g	1σ	µg/g	1σ	µg/g	1σ	µg/g	1σ	µg/g	1σ	µg/g	1σ	µg/g	1σ
Ni	6.3	(38)	5.6	(18)	<8.09		13	(2)	26	(5)	24	(7)	29.4	(46)
Co	8.3	(9)	9.1	(4)	18	(2)	21	(1)	18	(1)	16	(1)	15.5	(8)

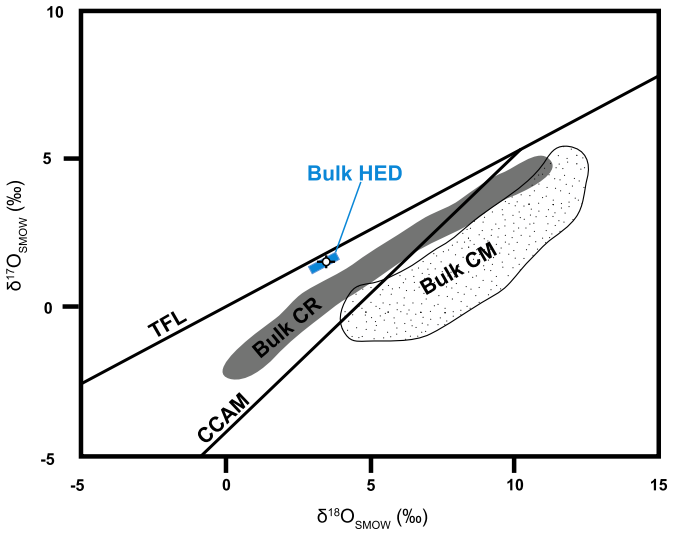

Fig. 3. Oxygen three-isotope compositions of Mg-rich olivine. The open circle is the average oxygen isotope composition for 47 Mg-rich olivine spot analyses on 16 grains: the error bars include 2σ standard error and the analytical uncertainty. The bulk HED field includes the eucrite fractionation line and bulk HED analyses, representing Vesta. TFL refers to the terrestrial fractionation line. CCAM refers to the carbonaceous chondrite anhydrous mineral line. Bulk CR and Bulk CM fields refer to bulk analyses of CR chondrites and CM chondrites, respectively. Oxygen three-isotope compositions of other meteorite groups are from Krot et al. (2006) and references therein.

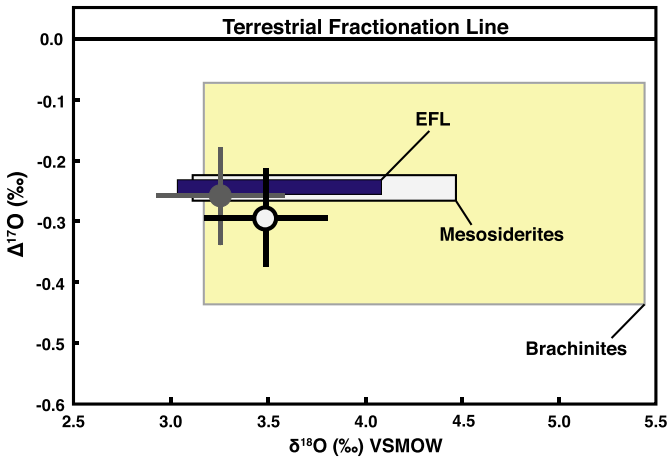

Fig. 4. Oxygen three isotope compositions of Mg-rich olivine and diogenite olivine determined in this study. The open circle is the average oxygen isotope composition for 47 Mg-rich olivine spot analyses on 16 grains. The filled gray circle is the average oxygen isotope composition for 34 diogenite olivine spot analyses on 14 grains. The error bars include 2σ standard error and the analytical uncertainty. The EFL is the eucrite fractionation line, which represents the HED meteorites associated with 4 Vesta. The EFL and oxygen isotope fields for other meteorite parent bodies are from data in Greenwood et al. (2012).

consistent with HED whole-rock analyses collected using laser fluorination methods (e.g., Greenwood et al., 2012; Day et al., 2012).

3.4. Trace element analyses

The Mg-rich olivines contain 6–52 ppm Ni and 5–26 ppm Co (Table 3). For the relatively incompatible trace elements we analyzed, the Mg-rich olivines are depleted relative to CI chondrites. For instance, in the Mg-rich olivine the Y concentration range is 0.03–0.37 ppm (Table A.3) and the CI-normalized Y range is 0.02–0.24. REE in the Mg-rich olivine are depleted relative to CI chondrites and frequently do not have concentrations above analytical detection limits (Table A.3), which are all below CI chondrite REE concentrations.

Two of the Mg-rich pyroxene grains analyzed (Mg# = 91.9 and 90.1) have Sr and LREE concentrations that are depleted relative to their HREE concentrations: CI-normalized La/Tm ratios = 0.02–0.04. The Mg# 91.9 and Mg# 90.1 pyroxenes have CI-chondrite normalized Eu/[(Sm + Gd)/2] = Eu/Eu* ratios of 0.1 and 0.2, respectively; these negative Eu anomalies exceed the 1σ errors on Sm, Eu, and Gd. CI-normalized La, Ce, and Pr concentrations of these 2 pyroxenes (Mg# = 91.9 and 90.1) are within 1σ errors of each other, and therefore do not have detectable Ce anomalies: Ce/[(La + Pr)/2] = Ce/Ce* (Fig. 5; Table 4; Table A.4). The REE patterns of these 2 Mg-rich pyroxenes (Mg# = 91.9 and 90.1) are reliable sources of petrologic processes because they do not have Ce anomalies (Floss and Crozaz, 1991), and they exhibit patterns of HREE enrichment relative to LREE that are typical of pyroxene.

In the other two Mg-rich pyroxenes (Mg# = 88.8 and 85.0) analyzed, the pattern of LREE depletion relative to HREE is not evident or is less pronounced (CI-normalized La/Tm ratios ≥0.09). These particular pyroxenes appear to have negative Ce anomalies: Mg# = 85.0 pyroxene has a Ce/Ce* = 0.26 and Mg# = 88.8 pyroxene has Ce/Ce* = 0.14; however, the latter anomaly represents the maximum possible anomaly because the La concentration is below 1σ detection limit so we used the La 1σ detection limit to calculate this Ce anomaly (Fig. 5; Tables 4 and A.4). We chose not to use data from these particular pyroxenes (Mg# = 88.8 and 85.0) to interpret petrologic processes, as they have Ce anomalies consistent with Antarctic weathering (which is not necessarily apparent in major element chemistry but mobilizes REE; Floss and Crozaz, 1991). The fact that they do not have the typical pyroxene HREE enrichment relative to LREE is further evidence that their REE may have been mobilized by terrestrial weathering.

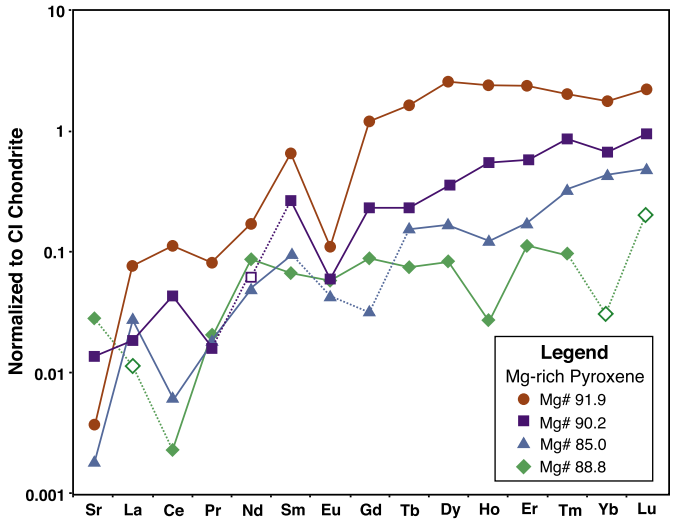

Fig. 5. Trace element patterns of Mg-rich pyroxene fragments from GRO 95 howardites. Closed symbols represent concentrations above 1σ limit of detection (LOD). The source data for this plot are listed in Tables 4 and A.4. Open symbols correspond to elements for which the analyses were below the 1σ LOD, and therefore each open symbol marks a maximum value, the 1σ LOD. When two adjacent data points represent values that are both above the LOD they are connected by a solid line, and dashed lines are used to connect concentrations that were determined based on an LOD.

4. Discussion

The Mg-rich olivine fragments are not restricted to the howardites we studied: olivine fragments with Mg#s = 80–92 have been noted in at least 9 other howardites (Delaney et al., 1980; Beck et al., 2012; Desnoyers, 1982; Fuhrman and Papike, 1981; Ikeda and Takeda, 1985; Shearer et al., 2010). Thus, the Mg-rich olivine is likely from a lithology broadly mixed into the vestan regolith.

4.1. HED–Vesta parent body provenance

To rigorously establish their vestan provenance, the Mg-rich olivines must be distinguished from olivines found in exogenic chondritic clasts within howardites. The most common exogenic components in howardites are clasts of CM and CR chondrites, and olivine grains in CM and CR chondrites are predominately very Mg-rich with Mg# = 97–100 (e.g., Tenner et al., 2015; Gounelle et al., 2003). A few percent of CM chondrite-like material has been inferred in Vesta's regolith via remote sensing of spatially correlated H- and OH-bearing dark materials by the DAWN spacecraft (e.g., De Sanctis et al., 2013; Prettyman et al., 2012).

To assess parent body origin, we used Fe/Mn ratios in olivine and pyroxene because they fall within specific ranges for differentiated parent bodies (Papike et al., 2003). The Mg-rich olivines in GRO 95 howardites have Fe/Mn = 37–45 (Fig. 2, Table 1) and are consistent with vestan olivine Fe/Mn = 40–60 (Beck et al., 2012), within analytical uncertainty. The Mg-rich pyroxene fragments have Fe/Mn = 23–32 (Table 2) in agreement with the range of Fe/Mn reported for vestan pyroxene (Mittlefehldt et al., 1998), Fe/Mn = 23–40.

To further constrain the parent body provenance, we analyzed oxygen three-isotope compositions of olivine (Goodrich et al., 2010). The average GRO 95 Mg-rich olivine oxygen isotope composition does not overlap those of CR and CM chondrites

Table 4
Trace element chemistry of Mg-rich olivine from GRO 95 howardites determined by LA ICP-MS. 1σ refers to the error of the analyses calculated by the SILLS program using the Longerich method (Guillong et al., 2008). 1σ is given in terms of the last decimal place, for instance 74 ± 3 is listed as 74 (3). Mg# listed in this table were calculated from EMPA (Table 2).

	GRO 95534,4		GRO 95535,16		GRO 95574,17		GRO 95581,7	
Grain	MgPx8		MgPx2		MgPx1		MgPx1	
Mg#	91.9		85.0		90.2		88.8	
	µg/g	1σ	µg/g	1σ	µg/g	1σ	µg/g	1σ
Sc	74	(3)	60	(1)	77	(2)	58	(2)
Ti	934	(35)	306	(3)	436	(11)	55	(2)
V	142	(6)	73	(1)	113	(2)	37	(1)
Co	7.0	(5)	13.7	(2)	7.7	(5)	6.4	(3)
Ni	4.8	(30)	5.0	(10)	3.3	(14)	8.4	(12)
Ga	0.28	(8)	0.090	(23)	0.250	(52)	0.036	(28)
Sr	0.030	(17)	0.015	(6)	0.110	(15)	0.225	(16)
Y	3.12	(17)	0.224	(13)	0.738	(34)	0.088	(11)
Zr	6.81	(29)	0.075	(15)	0.377	(42)	0.027	(13)
Nb	0.158	(48)	<0.00605		<0.0133		<0.00808	
Ba	0.020	(6)	<0.00183		0.0053	(44)	0.0099	(21)
La	0.018	(11)	0.0065	(41)	0.0045	(46)	<0.00266	
Ce	0.068	(16)	0.0036	(23)	0.0270	(63)	0.0014	(21)
Pr	0.0142	(77)	0.0031	(16)	0.0028	(31)	0.0035	(9)
Nd	0.080	(68)	0.023	(16)	<0.0287		0.040	(21)
Sm	0.097	(43)	0.0143	(85)	0.039	(19)	<0.0100	
Eu	0.0061	(77)	<0.00237		0.0034	(38)	0.0033	(30)
Gd	0.243	(78)	<0.00601		0.048	(28)	0.0181	(63)
Tb	0.059	(14)	0.0057	(18)	0.0086	(50)	0.0027	(20)
Dy	0.614	(92)	0.0408	(86)	0.087	(29)	0.020	(11)
Ho	0.133	(18)	0.0069	(25)	0.0321	(51)	0.0016	(22)
Er	0.362	(48)	0.0269	(67)	0.094	(18)	0.0179	(43)
Tm	0.048	(13)	0.0079	(20)	0.0210	(51)	0.0023	(34)
Yb	0.292	(46)	0.069	(11)	0.108	(26)	<0.00483	
Lu	0.054	(18)	0.0113	(50)	0.024	(10)	<0.00479	
Hf	0.257	(37)	0.0070	(53)	0.0110	(94)	0.0101	(43)
Ta	0.0056	(85)	<0.000780		<0.00507		<0.00227	
W	0.010	(17)	0.0066	(31)	<0.00718		<0.00756	
Pb	0.116	(42)	0.0260	(92)	0.059	(26)	0.017	(15)
Th	0.0159	(71)	<0.00105		<0.00215		<0.000822	
U	0.0049	(36)	<0.000462		0.0032	(21)	0.0017	(13)

(Fig. 3). However, the average Mg-rich olivine oxygen isotope composition (Fig. A.1, Table A.1) overlaps those of the brachinite, mesosiderite, and HED (vestan) meteorites (Greenwood et al., 2012; Day et al., 2012). The brachinite parent body can be eliminated as the source of Mg-rich olivine because brachinite olivines are more Fe-rich (Mg# = 65–71) and have higher Fe/Mn ratios (>59) (Gardner-Vandy et al., 2013). The mesosiderite parent body can also be eliminated as a source because the Mg-rich olivines analyzed in GRO 95 howardites have about an order of magnitude less Ni (6–52 ppm Ni), when compared to most mesosiderite olivines (88–980 ppm Ni; Kong et al., 2008; Powell, 1971). Therefore, the oxygen isotope and elemental chemistry of the Mg-rich olivine fragments are consistent with a vestan origin, and are not consistent with other possible sources.

In addition to major element ratios and oxygen isotope ratios, siderophile elemental abundances in olivine can be used to examine parent body provenance. The concentrations of Ni and Co in GRO 95 Mg-rich olivines (6–52 ppm and 5–26 ppm, respectively; Table 3) overlap abundances estimated for the bulk vestan mantle (4–80 ppm and 7–40 ppm, respectively; Righter and Drake, 1997). Since Ni and Co are compatible in olivine, the similarity between their concentrations in the Mg-rich olivine and the estimated bulk composition of an olivine-dominated vestan mantle (Mandler and Elkins-Tanton, 2013; Ruzicka et al., 1997) is consistent with an interpretation that the Mg-rich olivine represent fragments of Vesta's mantle.

4.2. Petrogenesis of Mg-rich olivine

The Mg#s of the GRO 95 Mg-rich olivine fragments resemble those expected for the mantles of differentiated rocky bodies, which formed from chondritic composition precursors (e.g., Ruzicka et al., 1997). Olivine with Mg#s overlapping these mantle compositions can sometimes form in Mg-rich basalts or crustal layered intrusions, such as those respectively in Mg-rich basaltic dikes through the Rum ultramafic complex (Kent, 1995) and in the lunar Mg-rich suite (Shearer and Papike, 2005). These alternative scenarios invoke processes that would produce lithologies that have not been recognized in HED meteorites nor predicted by petrologic models. Regarding Mg-rich basalts, olivine is rare and Fe-rich (e.g., Mg# = 18; Delaney et al., 1980) in basaltic eucrites. Basaltic eucrites are also MgO-poor compared to terrestrial basalts that contain non-xenolithic Mg-rich olivine. Mg-rich olivine–phyric basalts/picrites have bulk rock ~15 wt.% MgO (e.g., Kent, 1995; Larsen and Pedersen, 2000); whereas, basaltic eucrites have bulk rock 5.5–9.2 wt.% MgO (Kitts and Lodders, 1998). Mg-rich olivine phenocrysts in basalts typically exhibit major element zoning, which is not present in the GRO 95 Mg-rich olivines. It is important to note, that in addition to the lack of Mg-rich basaltic HED meteorites, generation of Mg-rich basaltic/picritic melts would require substantially more heterogeneous serial magmatism on Vesta than included in current models (i.e., Mandler and Elkins-Tanton, 2013).

Regarding a scenario involving Mg-rich olivines forming as cumulate minerals, the lunar Mg-rich suite is an analogous fractionally-crystallized assemblage of dunites, harzburgites, pyroxenites, spinel troctolites, troctolites, norites, and gabbronorites (Shearer and Papike, 2005). The Co concentrations of olivine in the lunar Mg-rich suite (37–160 ppm Co; Table 3) exceed those in the GRO 95 Mg-rich olivine (5–26 ppm Co: Table 3). The lunar Mg-rich suite ultramafic lithologies and spinel troctolites contain Mg-rich olivine (Mg# = 85–90 and Mg# = 90–93 respectively), but the olivines in these lithologies are more Ni-rich (108–291 and 92–107 ppm respectively) than the GRO 95 Mg-rich olivine (6–52 ppm Ni; Table 3). As we later discuss, vestan mantle minerals are expected to be relatively low in compatible siderophile elements such as Ni and Co because they are thought to be in equilibrium with core-forming FeNi metal liquids. The olivines in the lunar Mg-rich suite norites and gabbronorites are more Fe-rich (Mg# = 70–78 and Mg# = 66–77 respectively). However, the olivines in the lunar Mg-rich suite troctolites (Mg# = 80–90 and 28–113 ppm Ni) overlap the Mg- and Ni-content of the GRO 95 Mg-rich olivine. The whole rock chemistries of the lunar Mg-rich suite are enriched in incompatible elements (relative to chondrites), indicative of crustal contamination of their parental melts, but the olivine does not consistently record crustal contamination. For example, in the lunar Mg-rich suite lithologies with olivine Mg# > 80, the Y concentrations vary from 0.07–61 ppm (CI-normalized 0.04–39; Shearer and Papike, 2005). For comparison, the GRO 95 Mg-rich olivines have 0.03–0.37 ppm Y (Table A.3) and thus do not record crustal contamination.

Given the nature of our olivine samples as fragmental clasts without additional petrologic context, we cannot definitively eliminate the possibility that the GRO 95 Mg-rich olivine originated in crustal layered intrusion or a Mg-rich basalt. However, there is no additional evidence that the GRO 95 Mg-rich olivine formed in a crustal intrusion or basalt. Conversely, the relatively low concentrations of compatible siderophile elements (Ni and Co) provide additional supporting evidence that the Mg-rich GRO 95 olivine formed in the vestan mantle.

The Ni and Co concentrations (6–52 ppm Ni and 5–26 ppm Co) in the Mg-rich olivine are consistent with modeled estimates for the vestan mantle (Righter and Drake, 1997) and with formation in an olivine-dominated lithology in chemical equilibrium with FeNi metal. Buseck and Goldstein (1969) cited the Ni concentrations in pallasite olivine (10 s of ppm) as evidence that the olivines formed in the deep interior/mantle of their parent body. Although Ni is compatible in olivine, Ni more readily partitions into FeNi metal by factors of 100–1000 (e.g., Ehlers et al., 1992). If the Mg-rich olivine originates from Vesta's mantle, it is more likely to have been in equilibrium with metal, either as part of the lower mantle in contact with the core or with metallic liquid that descended through olivine residues to form the core during differentiation. In contrast to the Mg-rich olivine, the ranges of olivine Ni content extend to higher concentrations in diogenites (6.3–277 ppm; Shearer et al., 2010) and mesosiderites (88–980 ppm Ni; Kong et al., 2008; Powell, 1971). The moderately higher Ni-concentrations in some diogenite and mesosiderite olivines are consistent with the hypothesized formation of these two lithologies in the upper mantle and/or lower crust away from FeNi metals (Shearer et al., 2010; Powell, 1971). Diogenites occasionally contain accessory tetrataenite (ordered FeNi), but olivine is frequently the mineral phase into which Ni would have most readily partitioned. Further, a moderate abundance of Ni in diogenite parental melts may be explained by post-core formation accretion of chondritic material to Vesta (Day et al., 2012).

4.3. Mantle of Vesta: magma ocean or partially melted?

Although other possible origins cannot be completely eliminated, a mantle origin for the GRO 95 Mg-rich olivine fragments is the only petrogenetic scenario supported by multiple lines of evidence: Ni content consistent with equilibrium with FeNi metal and Mg#s that span almost the entire range predicted by whole-mantle magma ocean models for Vesta.

To date, no single vestan mantle model can fully account for the characteristics of Mg-rich olivines and diogenites. For instance, equilibrium crystallization models invoking whole-mantle magma ocean crystallization (e.g., Mandler and Elkins-Tanton, 2013; Righter and Drake, 1997) inherently predict narrower ranges in olivine Mg# than those measured here. Alternatively, the model of Ruzicka et al. (1997), which invokes fractional crystallization and

crystal settling in a whole-mantle magma ocean, predicts olivines with Mg#s ranging from 80–93, similar to the range among GRO 95 Mg-rich olivine fragments (Mg# = 80–92). However, this fractional crystallization model cannot produce magmas that would lead to formation of the diogenites (McCoy et al., 2006).

As a result of the shortcomings of equilibrium and fractional crystallization whole-mantle magma ocean models, we hypothesize that the vestan mantle experienced incomplete melting, similar to that described by the models of Wilson and Keil (2013) and Neumann et al. (2014) in which differentiation occurs in the absence of a whole-mantle magma ocean. Such partial melting would produce olivine residues with a wide range of Mg-compositions, as observed among GRO 95 Mg-rich olivines. In addition, complementary partial melts could have fractionally crystallized Mg-rich pyroxene (and some olivine) with compositions that may have graded into the well-established range for the diogenites.

Regarding pyroxene, in whole-mantle magma ocean models (e.g., Righter and Drake, 1997; Mandler and Elkins-Tanton, 2013; Ruzicka et al., 1997), the most Mg-rich pyroxenes have Mg#s $\leq$ 84. Such results do not match the GRO Mg-rich pyroxenes, which have Mg# = 85–92. Further, and regardless of whether equilibrium or fractional crystallization dominates, vestan whole-mantle magma ocean models consistently predict that large quantities of Mg-rich olivine will crystallize *before* progressively lower Mg-content pyroxene and olivine co-crystallize (Righter and Drake, 1997; Mandler and Elkins-Tanton, 2013; Ruzicka et al., 1997). When Mg-rich olivine and pyroxene do co-crystallize, Mg#s of pyroxene are typically greater than or equal to those of olivine (Beck and McSween, 2010 and references therein). Thus, based on their Mg#s, we hypothesize that the Mg-rich pyroxene (Mg# = 85–92) could have co-crystallized with at least some Mg-rich olivine. Lending support to this hypothesis is the observation that one of the Mg-rich pyroxene fragments (Mg# = 88.8) includes a small ($\sim$5 μm-wide) intergrown grain of Mg-rich olivine (Mg# = 86.9).

Two Mg-rich pyroxene grains, with Mg# 91.9 and Mg# 90.1, indicate that they co-crystallized with plagioclase or in the presence of Al-rich liquids. These two Mg-rich pyroxene grains have Eu and Sr depletions (Fig. 5). Further, these Mg-rich pyroxenes have negative Eu anomalies (Eu/Eu* ratios of 0.1 and 0.2: Table A.4) that are comparable to those from diogenite pyroxenes that co-exist with plagioclase (Shearer et al., 2006; Beck et al., 2013b). As such, the co-crystallization of these particular GRO 95 pyroxenes with plagioclase or co-existent Al-rich liquids could explain their Sr and Eu depletions. For reference, plagioclase preferentially incorporates both Eu and Sr at an oxygen fugacity expected for vestan magmatic systems ($\sim$IW-2: Righter and Drake, 1997). In addition, higher Al-contents of co-existing melt would increase negative Eu anomalies in pyroxene (Shearer et al., 2006). Alternatively, basaltic interstitial liquid among cumulate pyroxene could deplete orthopyroxene of Eu by subsolidus reactions, where depletions are positively correlated to the proportion of trapped melt (Barrat, 2004); such a process typically involves co-existing plagioclase, but can also include other phases that preferentially partition Eu, such as some phosphates (Shearer et al., 2006; Barrat, 2004). We note that pyroxene crystallizing without plagioclase does fractionate Eu slightly more than most other REE, but this partitioning is greater for high-Ca pyroxene (augite) than for the low-Ca Mg-rich pyroxene (orthopyroxene) we analyzed in this study.

If the initial fractional crystallization of mantle partial melts included plagioclase or trapped Al-rich liquid, as suggested by Eu and Sr anomalies in some GRO 95 pyroxenes, the vestan mantle would have incorporated ^{26}Al, thereby retaining some portion of the radiogenic heat source present in the early solar system (McCoy et al., 2006); this would have enabled the mantle to remain partially molten longer than it would have without this additional heat source. However, only very minor quantities of plagioclase or trapped Al-rich liquids in the mantle can be reconciled with (1) the relatively low bulk Al content calculated for Vesta's silicate fraction from a chondritic precursor (Toplis et al., 2013), and (2) the concept that most Al would have been extracted from the mantle by ascending basaltic magmas (Righter and Drake, 1997). For reference, a chondritic composition is the most appropriate estimate of Vesta's precursor material, especially in light of the calculation of Vesta's FeNi core mass fraction from geophysical data collected by the Dawn spacecraft (Russell et al., 2013), which falls within the range predicted by models using chondritic bulk compositions (Righter and Drake, 1997).

The suggestion that pyroxene co-crystallized with plagioclase or Al-rich liquid, based on pyroxene Eu and Sr anomalies, is consistent with differentiation by incomplete melting, rather than whole-mantle magma ocean models. For smaller planetesimals (diameters $\leq$100 km), partial melting is the most likely mechanism that drove differentiation, and it has been proposed that even in Vesta-sized bodies (diameter $\approx$500 km) rapid magma ascent could preclude a fully molten mantle (Wilson and Keil, 2013). Alternatively, Vesta could have produced a shallow magma ocean, leaving an olivine-rich solid residue in Vesta's lower mantle (Neumann et al., 2014). Partial melting models, with or without a shallow magma ocean, are easy to reconcile with a broad range of Mg-rich olivine compositions, and are more consistent with Mg-rich pyroxene fractionally crystallizing out of mantle partial melts. Thus, when compared to whole-mantle magma ocean models, partial melting can more reasonably generate magmas that are sufficiently enriched in Al to crystallize Mg-rich pyroxene showing Eu and Sr depletions.

5. Conclusions

The Mg-rich olivine fragments found in the GRO 95 howardites do not correspond to any established HED lithology. They may be the first recognized mantle olivine from Vesta, the HED parent body. Other petrogenetic scenarios that might account for the Mg#s, such as formation in crustal layered intrusions or in Mg-rich basalts, cannot be unequivocally eliminated. However, the relatively low Ni and Co concentrations (6–52 ppm Ni and 5–26 ppm Co) lend additional support that the GRO 95 Mg-rich olivine formed as mantle residues.

The GRO 95 Mg-rich olivines are not exogenic. They share parent body signatures with other HED meteorites:

- Fe/Mn ratios are consistent with other HED olivines and pyroxenes.
- Oxygen three-isotope composition of Mg-rich olivine overlap compositions for other HED (diogenite) olivine analyzed in this study, as well as bulk rock values in previous studies.
- Major element chemistries and Ni contents definitively distinguish these olivines from the other meteorite parent bodies with oxygen three-isotope ranges that overlap the HEDs.

Beyond their distinctive Mg#s and siderophile element concentrations, interpreted as evidence for a mantle origin, the Mg-rich olivines contain chemical signatures that imply the mantle of Vesta did not form from an equilibrated whole-mantle magma ocean; instead, their signatures are more consistent with a mantle dominated by partial melting and serial magmatism, perhaps producing a shallow magma ocean. Specifically, the wide range in Mg#s of the Mg-rich olivines indicates that the mantle of Vesta contained regions that experienced different degrees of partial melting and were not in chemical communication with each other.

Additionally, two of the Mg-rich pyroxenes (Mg#s 91.9 and 90.1) were likely in contact with an Al-rich liquid, based on depletions in Eu and Sr, which suggest they co-crystallized with plagioclase. Thus, these Mg-rich pyroxenes likely crystallized from

mantle partial melts and may correspond to the most primitive end members of the diogenite suite. However, Mg-rich olivine and pyroxene co-exist, and provide evidence that the boundaries may not be sharp between the earliest products of fractional crystallization from mantle partial melts and the residues from which those melts were extracted.

Author contributions

NGL and HYM developed and planned this study. NGL conducted EMP analyses and lithologic distribution mapping at the University of Tennessee, Knoxville. TJT, NTK, and NGL conducted SIMS analyses at the University of Wisconsin, Madison. NGL and RJB conducted LA-ICP-MS analyses at Virginia Tech. NGL wrote the manuscript with input from HYM, TJT, NTK, and RJB.

Acknowledgements

We thank the Meteorite Working Group for allocation of thin sections, Allan Patchen for assistance with EMPA, and Luca Fedele for assistance with LA-ICP-MS analyses. We thank an anonymous reviewer and Dr. Sara Russell for constructive comments. The data presented in this paper are available in the Online Supplementary Material. This research was supported in part by NASA through NNX13AH86G to HYM and NNX11AG62G to NTK. WiscSIMS is partly supported by NSF (EAR10-53466).

Appendix A. Supplementary material

Supplementary material related to this article can be found online at http://dx.doi.org/10.1016/j.epsl.2015.02.043.

References

Ammannito, E., De Sanctis, M.C., Palomba, E., Longobardo, A., Mittlefehldt, D.W., McSween, H.Y., Marchi, S., Capria, M.T., Capaccioni, E., Frigeri, A., Pieters, C.M., Ruesch, O., Tosi, T., Zambon, F., Carroro, F., Fonte, S., Hiesinger, H., Magni, G., McFadden, L.A., Raymond, C.A., Russell, C.T., Sunshine, J.M., 2013. Olivine in an unexpected location on Vesta's surface. Nature 504, 122–125.

Barrat, J.-A., 2004. Determination of parental magmas of HED cumulates: the effects of interstitial melts. Meteorit. Planet. Sci. 39, 1767–1779.

Barrat, J.-A., Yamaguchi, A., Jambon, A., Bollinger, C., Boudouma, O., 2012. Low-Mg rock debris in howardites: evidence for KREEPy lithologies on Vesta? Geochim. Cosmochim. Acta 99, 193–205.

Beck, A.W., McSween, H.Y., 2010. Diogenites as polymict breccias composed of orthopyroxenite and harzburgite. Meteorit. Planet. Sci. 45, 850–872.

Beck, A.W., Welten, K.C., McSween, H.Y., Viviano, C.E., Caffee, M.W., 2012. Petrologic and textural diversity among the PCA 02 howardite group, one of the largest pieces of the vestan surface. Meteorit. Planet. Sci. 47, 947–969.

Beck, A.W., McCoy, T.J., Sunshine, J.M., Viviano, C.E., Corrigan, C.M., Hiroi, T., Mayne, R.G., 2013a. Challenges in detecting olivine on the surface of 4 Vesta. Meteorit. Planet. Sci. 48, 2155–2165.

Beck, A.W., McSween, H.Y., Bodnar, R.J., 2013b. In situ laser ablation ICP-MS analyses of dimict diogenites: further evidence for harzburgitic and orthopyroxenitic lithologies. Meteorit. Planet. Sci. 48, 1050–1059.

Burbine, T.H., McCoy, T.J., Miebom, A., Gladman, B., Keil, K., 2002. Meteoritic parent bodies: their number and identification. In: Bottke, W.F., Cellino, A., Paolicchi, P., Binzel, R.P. (Eds.), Asteroids III. University of Arizona Press, Tucson, AZ, pp. 653–667.

Buseck, P.R., Goldstein, J.I., 1969. Olivine compositions and cooling rates of pallasitic meteorites. Geol. Soc. Am. Bull. 80, 2141–2158.

Cartwright, J.A., Ott, U., Mittlefehldt, D.W., 2014. The quest for regolithic howardite. Part 2: surface origins highlighted by noble gases. Geochim. Cosmochim. Acta 140, 488–508.

Day, J.M., Walker, R.J., Qin, L., Rumble, D., 2012. Late accretion as a natural consequence of planetary growth. Nat. Geosci. 5, 614–617.

De Sanctis, M.C., Ammannito, E., Capria, M.T., Capaccioni, F., Combe, J.-P., Frigeri, A., Longobardo, A., Magni, G., Marchi, S., McCord, T.B., Palomba, E., Tosi, F., Zambon, F., Carraro, F., Fonte, S., Li, Y.-J., McFadden, L.A., Mittlefehldt, D.W., Pieters, C.M., Jaumann, R., Stephan, K., Raymond, C.A., Russell, C.T., 2013. Vesta's mineralogical composition as revealed by the visible and infrared spectrometer on Dawn. Meteorit. Planet. Sci. 48, 2166–2184.

Delaney, J.S., Nehru, C.E., Prinz, M., 1980. Olivine clasts from mesosiderites and howardites: clues to the nature of achondritic parent bodies. In: Proc. Lunar Planet. Sci. Conf., vol. 11, pp. 1073–1087.

Desnoyers, C., 1982. L'Olivine dans les howardites : origine, et implications pour le corps parent de ces meteorites achondritiques. Geochim. Cosmochim. Acta 46, 667–680.

Ehlers, K., Grove, T.L., Sisson, T.W., Recca, S.T., Zervas, D.A., 1992. The effect of oxygen fugacity on the partitioning of nickel and cobalt between olivine, silicate melt, and metal. Geochim. Cosmochim. Acta 56, 3733–3743.

Floss, C., Crozaz, G., 1991. Ce anomalies in the LEW85300 eucrite: evidence for REE mobilization during Antarctic weathering. Earth Planet. Sci. Lett. 107, 12–24.

Fuhrman, M., Papike, J.J., 1981. Howardites and polymict eucrite: regolith samples from the eucrite parent body. Petrology of Bholgati, Bununu, Kapoeta, and ALHA76005. In: Proc. Lunar Planet. Sci. Conf., vol. 12, pp. 1257–1279.

Gardner-Vandy, K.G., Lauretta, D.S., McCoy, T.J., 2013. A petrologic, thermodynamic and experimental study of brachinites: partial melt residues of an R chondrite-like precursor. Geochim. Cosmochim. Acta 122, 36–57.

Goodrich, C.A., Kita, N.T., Spicuzza, M.J., Valley, J.W., Zipfel, J., Mikouchi, T., Miyamoto, M., 2010. The Northwest Africa 1500 meteorite: not a ureilite, maybe a brachinite. Meteorit. Planet. Sci. 45, 1906–1928.

Gounelle, M., Zolensky, M.E., Liu, J.-C., Bland, P.A., Alard, O., 2003. Mineralogy of carbonaceous chondritic microclasts in howardites: identification of C2 fossil micrometeorites. Geochim. Cosmochim. Acta 67, 507–527.

Greenwood, R.C., Franchi, I.A., Gibson, J.M., Benedix, G.K., 2012. Oxygen isotope variation in primitive achondrites: the influence of primordial, asteroidal and terrestrial processes. Geochim. Cosmochim. Acta 94, 146–163.

Guillong, M., Meier, D.L., Allan, M.M., Heinrich, C.A., Yardley, B.W.D., 2008. SILLS: a MATLAB-based program for the reduction of laser ablation ICP-MS data of homogeneous materials and inclusions. In: Sylvester, P. (Ed.), Laser-Ablation-ICPMS in the Earth Sciences: Current Practices and Issues, vol. 40. Mineralogical Association of Canada, Quebec. Chap. A6.

Ikeda, Y., Takeda, H., 1985. A model for the origin of basaltic achondrites based on the Yamato 7308 howardite. J. Geophys. Res. Suppl. 90, C649–C663.

Jutzi, M., Asphang, E., Gillet, P., Barrat, J.-A., Benz, W., 2013. The structure of the asteroid 4 Vesta as revealed by models of planet-scale collisions. Nature 494, 207–210.

Larsen, L.M., Pedersen, A.K., 2000. Processes in high-Mg, high-T magmas: evidence from olivine, chromite and glass in paleogene picrites from west Greenland. J. Petrol. 41, 1071–1098.

Kent, R.W., 1995. Magnesian basalts from the Hebrides, Scotland: chemical composition and relationship to the Iceland plume. J. Geol. Soc. (Lond.) 152, 979–983.

Kita, N.T., Nagahara, H., Tachibana, S., Tomomura, S., Spicuzza, M.J., Fournelle, J.H., Valley, J.W., 2010. High precision SIMS oxygen three isotope study of chondrules in LL3 chondrites: role of ambient gas during chondrules formation. Geochim. Cosmochim. Acta 74, 6610–6635.

Kitts, K., Lodders, K., 1998. Survey and evaluation of eucrite bulk compositions. Meteorit. Planet. Sci. 33, A197–A213.

Kong, P., Su, W., Li, X., Spettel, B., Palme, H., Tao, K., 2008. Geochemistry and origin of metal, olivine clasts, and matrix in the Dong Ujimquin Qi mesosiderite. Meteorit. Planet. Sci. 43, 451–460.

Krot, A.N., Keil, K., Scott, E.R.D., Goodrich, C.A., Weisberg, M.K., 2006. Classification of meteorites. In: Davis, A.M. (Ed.), Meteorites, Comets, and Planets. 2nd edition. In: Treatise on Geochemistry, vol. 1. pp. 1.05-1–1.05-43.

Mandler, B.E., Elkins-Tanton, L.T., 2013. The origin of eucrites, diogenites, and olivine diogenites: magma ocean crystallization and shallow magma chamber processes on Vesta. Meteorit. Planet. Sci. 48, 2333–2349.

McCoy, T.J., Mittlefehldt, D.W., Wilson, L., 2006. Asteroid differentiation. In: Lauretta, D.S., McSween, H.Y., Binzel, R.P. (Eds.), Meteorites and the Early Solar Systems II. University of Arizona Press, Tucson, AZ, pp. 733–745.

McSween, H.Y., Ammannito, E., Reddy, V., Prettyman, T.H., Beck, A.W., De Sanctis, M.C., Nathues, A., Le Corre, L., O'Brien, D.P., Yamashita, N., McCoy, T.J., Mittlefehldt, D.W., Toplis, M.J., Schenk, P., Palomba, E., Turrini, D., Tosi, F., Zambon, F., Longobardo, A., Capaccioni, F., Raymond, C.A., Russell, C.T., 2013a. Composition of the Rheasilvia basin, a window into Vesta's interior. J. Geophys. Res. 118, 335–346.

McSween, H.Y., Binzel, R.P., De Sanctis, M.C., Ammannito, E., Prettyman, T.H., Beck, A.W., Reddy, R., Le Corre, L., Gaffey, M.J., McCord, T.B., Raymond, C.A., Russell, C.T., 2013b. Dawn, the Vesta–HED connection; and the geologic context for eucrite, diogenites, and howardites. Meteorit. Planet. Sci. 48, 2090–2104.

Mittlefehldt, D.W., McCoy, T.J., Goodrich, C.A., Kracher, A., 1998. Non-chondritic meteorites from asteroidal bodies. In: Papike, J.J. (Ed.), Planetary Materials, vol. 39. Mineralogical Society of America, Washington, DC. Chap. 4.

Mutchler, S.R., Fedele, L., Bodnar, R.J., 2008. Analysis Management System (AMS) for reduction of laser ablation ICP-MS data. In: Sylvester, P. (Ed.), Laser-Ablation-ICPMS in the Earth Sciences: Current Practices and Issues, vol. 40. Mineralogical Association of Canada, Quebec. Chap. A5.

Neumann, W., Breuer, D., Sophn, T., 2014. Differentiation of Vesta: implications for a shallow magma ocean. Earth Planet. Sci. Lett. 395, 267–280.

Papike, J.J., Karner, J.M., Shearer, C.K., 2003. Determination of planetary basalt parentage: a simple technique using the electron microprobe. Am. Mineral. 88, 469–472.

Powell, B.N., 1971. Petrology and chemistry of mesosiderites—II. Silicate textures and compositions and metal–silicate relationships. Geochim. Cosmochim. Acta 35, 5–34.

Prettyman, T.H., Mittlefehldt, D.W., Yamashita, N., Lawrence, D.J., Beck, A.W., Feldman, W.C., McCoy, T.J., McSween, H.Y., Toplis, M.J., Titus, T.N., Tricarico, P., Reedy, R.C., Hendricks, J.S., Forni, O., Le Corre, L., Li, J.-Y., Mizzon, H., Reddy, V., Raymond, C.A., Russell, C.T., 2012. Elemental mapping by Dawn reveals exogenic H in Vesta's regolith. Science 338, 242–246.

Righter, K., Drake, M.J., 1997. A magma ocean on Vesta: core formation and petrogenesis of eucrites and diogenites. Meteorit. Planet. Sci. 32, 929–944.

Russell, C.T., Raymond, C.A., Jaumann, R., McSween, H.Y., De Sanctis, M.C., Nathues, A., Prettyman, T.H., Ammannito, E., Reddy, V., Preusker, F., O'Brien, D.P., Marchi, S., Denevi, B.W., Buckowski, D.L., Pieters, C.M., McCord, T.B., Li, J.-Y., Mittlefehldt, D.W., Combe, J.-P., Williams, D.A., Hiesinger, H., Yingist, R.A., Polanskey, C.A., Joy, S.P., 2013. Dawn completes its mission at 4 Vesta. Meteorit. Planet. Sci. 48, 2076–2089.

Ruzicka, A., Snyder, G.A., Taylor, L.A., 1997. Vesta as the howardite, eucrite and diogenite parent body: implications for the size of a core and for large-scale differentiation. Meteorit. Planet. Sci. 32, 825–840.

Shearer, C.K., Papike, J.J., 2005. Early crustal building processes on the moon: models for the petrogenesis of the magnesian suite. Geochim. Cosmochim. Acta 69, 3445–3461.

Shearer, C.K., Papike, J.J., Karner, J.M., 2006. Pyroxene europium valence oxybarometer: effects of pyroxene composition, melt composition and crystallization kinetics. Am. Mineral. 91, 1565–1572.

Shearer, C.K., Burger, P., Papike, J.J., 2010. Petrogenetic relationships between diogenite and olivine diogenites: implications for magmatism on the HED parent body. Geochim. Cosmochim. Acta 74, 4865–4880.

Sunshine, J.M., Bus, S.J., Corrigan, C.M., McCoy, T.J., Burbine, T.H., 2007. Olivine-dominated asteroids and meteorites: distinguishing nebular and igneous histories. Meteorit. Planet. Sci. 42, 155–170.

Tenner, T.J., Ushikubo, T., Kurahashi, E., Kita, N.T., Nagahara, H., 2013. Oxygen isotope systematics of chondrules phenocrysts from the CO3.0 chondrite Yamato 81020: evidence for two distinct oxygen isotopes reservoirs. Geochim. Cosmochim. Acta 102, 226–245.

Tenner, T.J., Nakashima, D., Ushikubo, T., Kita, N.T., Weisberg, M.K., 2015. Oxygen isotope ratios of FeO-poor chondrules in CR3 chondrites: influence of dust enrichment and H_2O during chondrule formation. Geochim. Cosmochim. Acta 148, 228–250.

Toplis, M.J., Mizzon, H., Monnereau, M., Forni, O., McSween, H.Y., Mittlefehldt, D.W., McCoy, T.J., Prettyman, T.H., De Sanctis, M.C., Raymond, C.A., Russell, C.T., 2013. Chondritic models of 4 Vesta: implications for geochemical and geophysical properties. Meteorit. Planet. Sci. 48, 2300–2315.

Wilson, L., Keil, K., 2013. Volcanic activity on differentiated asteroids: a review and analysis. Chem. Erde 72, 289–321.